



Macroscopic model of multidirectional pedestrian network flows

Elhabib Moustaid^a, Gunnar Flötteröd^{b,c,*}

^a AlgoDx Algorithm Diagnostics, Stockholm, Sweden

^b Department of Science and Technology, Linköping University, SE-601 74 Norrköping, Sweden

^c Swedish National Road and Transport Research Institute, Sweden



ARTICLE INFO

Article history:

Received 17 July 2019

Revised 10 December 2020

Accepted 16 December 2020

Available online 20 January 2021

Keywords:

Bidirectional fundamental diagram

Pedestrian flow modeling

Pedestrian intersections

Cell-transmission model

Kinematic waves

ABSTRACT

Pedestrian flow models are useful for the design and operation of pedestrian spaces. This article describes a macroscopic model of pedestrian flows through networks composed of bidirectional corridors that are connected by multidirectional intersections. The proposed model builds on an existing pedestrian bidirectional fundamental diagram to define bidirectional sending and receiving flows, and it relies on the incremental transfer principle to model bidirectional flows across nodes with an arbitrary number of adjacent links. The model is solved in a cell-transmission formulation that is in all of its unidirectional properties consistent with the kinematic wave model.

© 2021 The Authors. Published by Elsevier Ltd.

This is an open access article under the CC BY-NC-ND license

(<http://creativecommons.org/licenses/by-nc-nd/4.0/>)

1. Introduction

Modeling pedestrian motion and flows is a complex problem that can be treated at different levels of aggregation and with a focus on a wide range of phenomena. Helbing et al. (2001) state that short-term pedestrian movements are highly predictable. The practical interest in pedestrian modeling stems from the insight these models provide to the design and operations of pedestrian spaces. An important instance of pedestrian spaces are walkways that can be composed to describe environments such as malls, tube stations or hospitals (Løvås, 1994; Lee and Abdel-Aty, 2005; Thompson and Marchant, 1995; Gärder, 1989).

The present article starts out from an existing bidirectional pedestrian fundamental diagram (FD) that expresses flows as functions of densities, given a few measurable parameters. The article generalizes this FD to be applicable for spatially inhomogeneous densities at linear interfaces and complex intersections; this enables its use for pedestrian network simulation. A macroscopic continuum flow approach is pursued that focuses on the bidirectional dynamics of densities, flows and velocities but simplifies many aspects of individual walking processes, lane generation or collision avoidance. The implications of these modeling assumptions are discussed throughout the article, as the model is developed.

This document is structured as follows. Section 2 presents a literature review. Section 3 briefly reviews the FD of Flötteröd and Lämmel (2015). Section 4 develops bidirectional sending and receiving functions that are compatible with this FD. Section 5 presents a corresponding network node model with an arbitrary number of in- and outgoing links, relying

* Corresponding author at: Swedish National Road and Transport Research Institute, Sweden.

E-mail address: gunnar.flotterod@vti.se (G. Flötteröd).

on an extension of the unidirectional node model of [Flötteröd and Rohde \(2011\)](#). [Section 6](#) presents simulation studies with a bidirectional cell-transmission model and a comparison to a real dataset. [Section 7](#) summarizes the document.

2. Background and contribution

Pedestrian flows have been described in many different ways. [Zheng et al. \(2009\)](#) review cellular automata (CA), Social Force (SF) and fluid dynamic models. Different models focused on different phenomena (lanes, collision anticipation, routing) and different quantities (individual positions, aggregate densities, flows, velocities) in different walking scenarios ([Gupta and Pundir, 2015](#); [Schadschneider et al., 2018](#)). The following review focuses on literature relevant to the modeling and simulation of dynamic flows in bidirectional pedestrian networks.

2.1. Pedestrian flow modeling and simulation

Given that pedestrian flows emerge from the interactions of individual walkers, the use of microscopic simulation models is prominent in studying pedestrian flows. CA models have been used to study pedestrian phenomena from the late 1990s. CA models represent the walking space as a regular grid of possible pedestrian locations. They have been used to model both uni- and multidirectional flows. The model of [Blue and Adler \(2001\)](#) captures different walking phenomena, amongst them lane separation and interspersed flows. [Burstedde et al. \(2001\)](#) introduce a bidirectional stochastic CA model that accounts for long-ranged interactions using a floor field. The model captures lane generation in bidirectional pedestrian flows. The CA model of [Tajima et al. \(2002\)](#) extends the lattice gas model with pedestrian following behavior; their model generates a triangular FD as it is known from the vehicular traffic flow literature. [Wang and Chen \(2009\)](#) present a bidirectional pedestrian flow CA with position exchanges exhibiting credible macroscopic performance measures in all but very low densities. [Dias and Lovreglio \(2018\)](#) calibrate a unidirectional CA model at a corner from experimental data. [Flötteröd and Lämmel \(2015\)](#) derive a bidirectional FD by taking a continuous limit of an utmost simple CA; their model relies on an avoidance parameter representing the delay caused to a pedestrian by a pedestrian walking in the opposite direction. The model exhibits a good fit against both simulated data (from an SF model) and a real data set.

SF models as introduced by [Helbing and Molnár \(1995\)](#) model pedestrian motion as the movement of a particle that is exposed to social forces that are exerted by other pedestrians and physical obstacles. SF models have been used to study a wide range of pedestrian behaviors. [Shukla \(2010\)](#) extend the SF model by including velocity-dependent interaction forces. In addition, their model considers the interactions of pedestrians with both static and dynamic obstacles, rendering it applicable to the modeling of pedestrian-vehicle interactions. [Zanlungo et al. \(2011\)](#) propose a SF model that enables pedestrians to predict (and avoid) the place and time of an upcoming collision. This leads to an improved model performance when validated against an empirical data set of pedestrians crossing another pedestrian stream. [Chraïbi et al. \(2010\)](#) validate a generalized SF model against a unidirectional flow data set. [Chen et al. \(2018\)](#) summarize the SF model developments of the past three decades and assert their ability to capture complex pedestrian self-organizing phenomena.

Similarly to CA and SF models, agent-based models start out from simple rules at a microscopic level of pedestrian walking behavior and aim to reproduce complex patterns of possibly heterogeneous pedestrian flows. Examples are [Turner and Penn \(2002\)](#) and [Schelhorn et al. \(1999\)](#). The latter present a model in which agents (pedestrians) interact with both the physical environment and other pedestrians. Pedestrians with different profiles react differently to the environment. [Hussein and Sayed \(2017\)](#) present the calibration and validation of an agent-based simulation which accounts for agent heterogeneity and nontrivial behavioral rules. Using a real data set from a study in Vancouver, the model is demonstrated to reproduce collision avoidance behaviour as well as a triangular FD.

2.2. Unidirectional kinematic wave and cell-transmission models

The kinematic wave model (KWM) is broadly used in road traffic flow theory for capturing the spatiotemporal dynamics of traffic flow and congestion, including spill-back. The cell-transmission model (CTM) of [Daganzo \(1994\)](#) is frequently used to solve a space- and time-discrete KWM approximation; [Lebacque \(1996\)](#) further analyzes its numerical properties. [Smits et al. \(2015\)](#) presents a family of node models that allow to represent the propagation of flows resp. kinematic waves across point-like road intersections. This family includes the Incremental Node Model (INM) of [Flötteröd and Rohde \(2011\)](#), which specifies the instantaneous flows across a road intersection given boundary conditions represented in the form of upstream sending flows and downstream receiving flows.

CTMs have been used to model unidirectional pedestrian flows. [Asano et al. \(2007\)](#) propose a two-stage model where the first model captures pedestrian path choice and flow allocation to paths, and the second (CTM) model represents the physical propagation of pedestrian flows. [Guo et al. \(2011\)](#) present a CTM-based pedestrian network model capturing congestion build-up, spill-back, and dissipation.

2.3. Multidirectional pedestrian network flows

The movement of pedestrians and car drivers is similar in the sense that both attempt to minimize delay along their way. This renders the road traffic models presented immediately above a relevant starting point for the pedestrian case.

Multidirectional flows have been investigated through both models and empirical studies (Isobe et al., 2004; Takimoto et al., 2002). Lattice Automata models are used by Tajima et al. (2002) to study the emergence of patterns. Xie and Wong (2015) investigate empirically the effect of the angle at which pedestrian stream meet and finds strongest interactions when the angle is 135°. Zhang and Seyfried (2014), however, find no apparent differences between the crossing angles 90° and 180°.

In a single corridor or a link, flows are only bidirectional, meaning that two streams head in opposite directions. A number of empirical studies and controlled experiments exist for the case of corridors, often resulting in a triangular form FD such as the study of Feliciani and Nishinari (2016). In a network of pedestrian links, more directions are possible only in intersections. Zhang et al. (2011b) study empirical FDs under different conditions and show a substantial difference between a linear corridor and a merging T-junction especially at high densities. Further empirical and simulation studies of T-junctions comprise Zhang et al. (2011a); Tajima and Nagatani (2002); Peng and Chou (2011). Zhang et al. (2013) compare flows in a T-junction to that at a single corner, revealing differences in flows and velocities. Bode et al. (2019) calibrate three non-spatial node models against a dataset obtained in a four-leg intersection. Their analysis focuses on the model's structure, stochasticity and stability, excluding node interactions with the adjacent channels.

2.4. Contribution of the present article

Flötteröd and Lämmel (2015) observe that a bidirectional flow model can be written as a system of unidirectional but interconnected flows and exploit this insight in the formulation of an FD for *stationary* flow on a *linear* link. The present work relaxes these two limitations by proposing a model of spatiotemporally dynamic bidirectional flows in networks of arbitrary topology. This is enabled by (i) extending the stationary FD to a formulation of bidirectional sending and receiving functions at a linear interface, and (ii) further generalizing this formulation to network nodes with many connecting links, relying on a generalization of the unidirectional Incremental Node Model model (Flötteröd and Rohde, 2011). This allows to formulate a general-topology network cell-transmission model of dynamic bidirectional pedestrian flows that, due to its computational simplicity and limited number of parameters, bears potential for the simulation of large pedestrian facilities. Such models are useful for the planning and design of, for instance, inner-city pedestrian zones or indoor corridor systems.

3. Brief review of underlying fundamental diagram

Denote by ϱ the density of pedestrians walking in one direction through a corridor, and let ϱ' be the density of pedestrians walking in the opposite direction. Densities are uniform and stationary along the corridor; they are non-negative and do in their sum not exceed the jam density $\hat{\varrho}$ (maximum number of pedestrian that can fit in one unit of space):

$$\varrho + \varrho' \leq \hat{\varrho}. \quad (1)$$

Given the linear form of a corridor, density is measured in pedestrians per length unit, meaning that the lateral channel dimension (in particular, its width), is disregarded. One may, in symmetry to the vehicular single-lane case, assume channels that are as wide as one pedestrian. Once developed, the model carries over straightforwardly to different channel widths, as demonstrated in Section 6.2.3.

The bidirectional FD of Flötteröd and Lämmel (2015) predicts the flows given these densities, relying on three parameters: (i) jam density $\hat{\varrho}$, (ii) free walking speed \hat{v} , and (iii) a conflict delay parameter D that represents the delay experienced by a pedestrian encountering another pedestrian walking in the opposite direction. All three parameters are subsequently assumed to be strictly positive.

A unidirectional fundamental diagram differentiates between under- and overcritical flow, which arise when the unidirectional density is below resp. above a critical density (Lebacque, 1996). In generalization of this concept to the bidirectional case, the critical density ϱ^* is defined as a function of the counter-density ϱ' as follows:

$$\varrho^*(\varrho') = \begin{cases} \hat{\varrho} \cdot \frac{1 + D\hat{v}\varrho'}{2 + D\hat{v}\hat{\varrho}} & \text{if } \varrho' \leq \hat{\varrho}/2 \quad (2a) \\ \text{undefined} & \text{otherwise.} \quad (2b) \end{cases}$$

Fig. 1 (a) provides an illustration. Only density configurations in the shaded region comply with the jam density constraint (1). The thick solid line displays the critical density in flow direction of density ϱ as a function of the counter-density ϱ' . At all points (ϱ, ϱ') left (resp. right) of this line, the flow is undercritical (resp. overcritical). Symmetrically, the thick dashed line displays the critical density in flow direction of ϱ' as a function of the counter-density ϱ . The critical lines separate the feasible density configurations into three regions: SS (both densities are undercritical, i.e. in sending mode), RS (ϱ is overcritical, i.e. in receiving mode, and ϱ' is undercritical), and SR (ϱ is undercritical and ϱ' is overcritical).

Letting

$$w = \frac{\hat{v}}{1 + D\hat{v}\hat{\varrho}}, \quad (3)$$

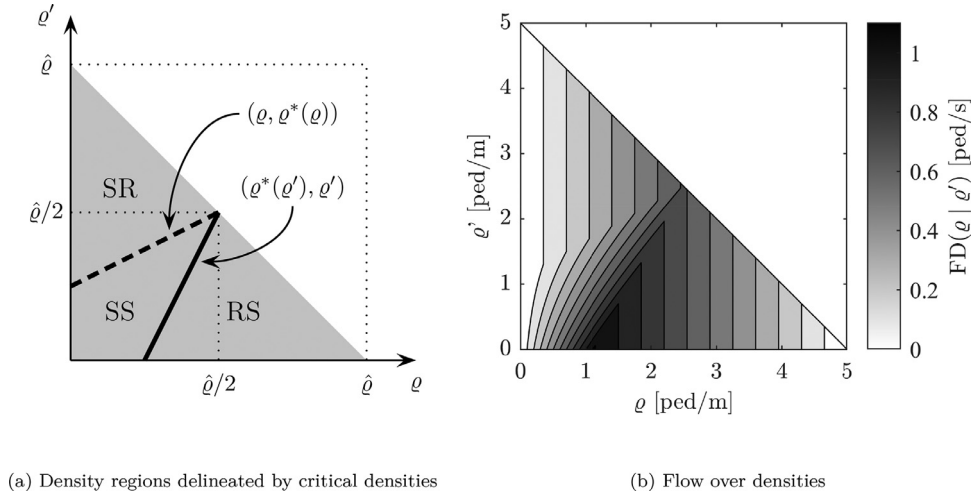


Fig. 1. Density regions and flows in bidirectional fundamental diagram.

the FD of Flötteröd and Lämmel (2015) models the flow in a given direction as a function of the corresponding density ρ given the counter-density ρ' as follows:

$$\text{FD}(\rho | \rho') = \begin{cases} w\rho & \text{if } \rho' \geq \rho^*(\rho) \text{ (SR regime)} & (4a) \\ w(\hat{\rho} - \rho) & \text{if } \rho \geq \rho^*(\rho') \text{ (RS regime)} & (4b) \\ \hat{v}\rho \cdot \frac{1+D\hat{v}(\rho-\rho')}{1+D\hat{v}(\rho+\rho')} & \text{otherwise (SS regime).} & (4c) \end{cases}$$

This function is illustrated in Fig. 1(b), using the parameters $\hat{v} = 1 \text{ m/s}$, $\hat{\rho} = 5 \text{ ped/m}$, $D = 0.5 \text{ s}$, with “ped” abbreviating “pedestrian”. The linear flow-density relationships in the SR and RS region are identifiable from the vertical contour lines. In-between, the non-linear relationship of the SS regime is visible.

The bidirectional FD collapses into a triangular unidirectional FD if the counter-density vanishes:

$$\text{FD}(\rho | 0) = \begin{cases} w(\hat{\rho} - \rho) & \text{if } \rho \geq \rho^*(0) \\ \hat{v}\rho & \text{otherwise} \end{cases} \quad (5)$$

$$= \min\{\hat{v}\rho, w(\hat{\rho} - \rho)\}. \quad (6)$$

The unidirectional backward wave speed w is hence not an independent parameter but given by (3). $\text{FD}(\rho | \rho')$ is for fixed $\rho' \in [0, \hat{\rho}/2]$ a uni-modal function of ρ that strictly increases for $\rho \in [0, \rho^*(\rho')]$ and strictly (and linearly) decreases for $\rho \in (\rho^*(\rho'), \hat{\rho} - \rho']$. For $\rho' \in [\hat{\rho}/2, \hat{\rho}]$, it is strictly (and linearly) increasing over all feasible ρ . For any fixed ρ , it is a monotonously decreasing function of the counter-density ρ' (more specifically, it is constant over the SR and RS regions and for $\rho = 0$, and it is strictly decreasing over the SS region apart from $\rho = 0$). These properties are confirmed in Appendix A.

4. Linear interface model

The FD (4a)-(4c) predicts spatially homogeneous flows as functions of spatially homogeneous densities. The problem considered here is to express the flows exchanged at an interface separating two adjacent links, with each link carrying spatially homogeneous bidirectional densities. This is a generalization of the unidirectional problem considered by Daganzo (1994); Lebacque (1996). In the unidirectional case, the flow across the interface is the minimum of an upstream sending and a downstream receiving function. A corresponding approach is chosen here, but defining both a sending and a receiving function on either side of the interface.

Given a counter-density ρ' , the FD (4a)-(4c) attains for $\rho' < \hat{\rho}/2$ its maximum (capacity) flow at the critical density $\rho^*(\rho')$. For $\rho' \geq \hat{\rho}/2$, the notion of a capacity flow appears meaningless because $\text{FD}(\rho | \rho')$ increases over all feasible density values ρ . The chosen specification (case (7b) below) can be given a physical meaning once the interface is defined in its entirety, i.e. in Section 4.1.2. The capacity flow is defined as the following function of the counter-density ρ' :

$$q^*(\rho') = \begin{cases} \text{FD}(\rho^*(\rho') | \rho') = w(\hat{\rho} - \rho^*(\rho')) & \text{if } \rho' \leq \hat{\rho}/2 & (7a) \\ \text{FD}(\hat{\rho}/2 | \hat{\rho}/2) = w\hat{\rho}/2 & \text{if } \rho' \geq \hat{\rho}/2. & (7b) \end{cases}$$

This function is continuous in ρ' .

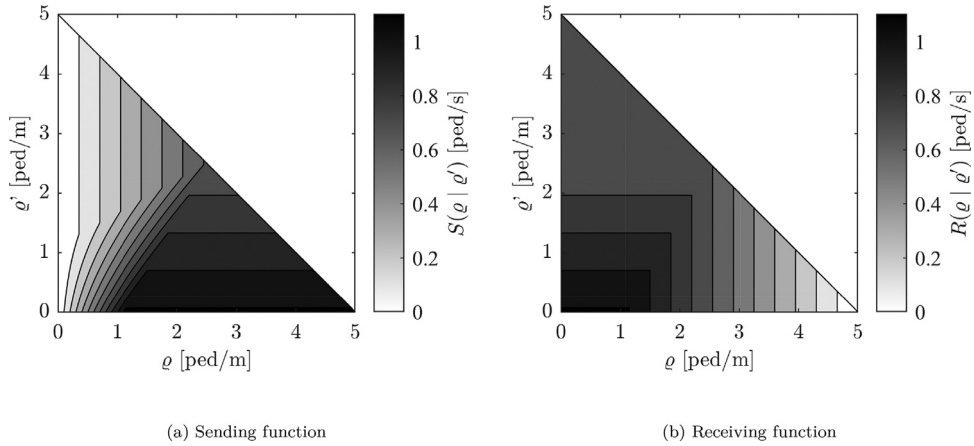


Fig. 2. Sending and receiving functions.

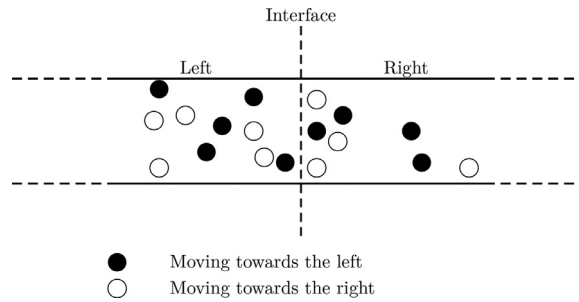


Fig. 3. Microscopic interpretation of interface flow.

4.1. Sending flow

The sending flow is the largest amount of flow that can be dismissed from one side of the interface towards the interface, given the density ρ of pedestrians moving towards the interface and the counter-density ρ' on the same side. It is defined through the following sending function:

$$S(\rho | \rho') = \begin{cases} \text{FD}(\rho | \rho') & \text{if } \rho \leq \rho^*(\rho') \text{ (under-critical)} & (8a) \\ q^*(\rho') & \text{if } \rho \geq \rho^*(\rho') \text{ (over-critical)}. & (8b) \end{cases}$$

In the first case, the density ρ that is ready to approach the interface is, given the counter-density ρ' , under-critical. The sending flow is hence set to the flow within the sending link, which is given by the fundamental diagram. The second case arises if ρ is overcritical, in which case the capacity flow limits what can be sent. Inserting expressions yields the following:

$$S(\rho | \rho') = \begin{cases} \hat{v}\rho \cdot \frac{1+D\hat{v}(\rho-\rho')}{1+D\hat{v}(\rho+\rho')} & \text{if } \rho \leq \rho^*(\rho') \text{ and } \rho' \leq \rho^*(\rho) & (9a) \\ w\rho & \text{if } \rho \leq \rho^*(\rho') \text{ and } \rho' \geq \rho^*(\rho) & (9b) \\ w(\hat{\rho} - \rho^*(\rho')) & \text{if } \rho \geq \rho^*(\rho'). & (9c) \end{cases}$$

Fig. 2(a) illustrates the sending function, using the same parameters as before. Its monotonicity properties are inherited from those of the FD in under-critical conditions: $S(\rho | \rho')$ increases monotonically with ρ and decreases monotonically with ρ' .

An interpretation in terms of microscopic processes is provided in Fig. 3. All flow that can leave the left link has to seep through the counter-flow already within that link. The sending flow from the left is the maximum amount of white particles that can move towards the interface, bounded by free flow speed, the counter-movement of black particles on the left, and by not being able to overtake preceding white particles on the left.

4.1.1. Receiving flow

The receiving flow is the largest amount of flow that can enter a link from the interface, given the receiving link's density ρ of pedestrians moving away from the interface and its counter-density ρ' . It is defined through the following receiving

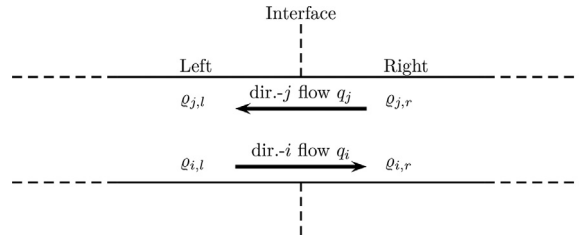


Fig. 4. Linear interface.

function:

$$R(\varrho \mid \varrho') = \begin{cases} q^*(\varrho') & \text{if } \varrho \leq \varrho^*(\varrho') \text{ (under-critical)} & (10a) \\ \text{FD}(\varrho \mid \varrho') & \text{if } \varrho \geq \varrho^*(\varrho') \text{ (over-critical)}. & (10b) \end{cases}$$

The first case captures an under-critical situation where the density ϱ is, relative to the counter-density ϱ' , low enough that the capacity flow can be received. The second case describes an over-critical situation where the already present ϱ limits the flow that can follow up from the interface. The receiving flow is hence set to the flow within the link, as given by the fundamental diagram. Inserting expressions (and noting that both directions cannot be overcritical at the same time), one obtains

$$R(\varrho \mid \varrho') = \begin{cases} w(\hat{\varrho} - \varrho^*(\varrho')) & \text{if } \varrho \leq \varrho^*(\varrho') \text{ and } \varrho' \leq \hat{\varrho}/2 & (11a) \\ w\hat{\varrho}/2 & \text{if } \varrho' \geq \hat{\varrho}/2 & (11b) \\ w(\hat{\varrho} - \varrho) & \text{if } \varrho \geq \varrho^*(\varrho') \text{ (implying } \varrho' \leq \hat{\varrho}/2). & (11c) \end{cases}$$

The receiving function is illustrated in Fig. 2(b), using the same parameters as before, and again with monotonicity properties inherited from the underlying FD: $R(\varrho \mid \varrho')$ decreases monotonically with both ϱ and ϱ' . Fig. 3 provides microscopic intuition. All white particles having crossed the interface towards the right have to seep through the black counter-flow particles in the right link, and they may additionally be held back by preceding white particles that are already within the right link.

4.1.2. Interface flow specification and properties

The following notation is introduced in Fig. 4: l resp. r refers to the left- resp. right-hand side (abbreviated l.h.s. resp. r.h.s.) of the interface. i indicates the flow direction $l \rightarrow r$, and j indicates the direction $l \leftarrow r$. For instance, a density located left of the interface and moving towards the right is denoted by $\varrho_{i,l}$, the corresponding sending flow is written as $S_{i,l}$, and the resulting flow across the interface is denoted by q_i .

In symmetry to the unidirectional case, the interface flow is defined as the minimum of an upstream sending function and a downstream receiving function, with the notions of “upstream” and “downstream” now being direction-dependent. For direction i :

$$Q(\varrho_{i,l}, \varrho_{i,r} \mid \varrho_{j,l}, \varrho_{j,r}) = \min\{S(\varrho_{i,l} \mid \varrho_{j,l}), R(\varrho_{i,r} \mid \varrho_{j,r})\}. \quad (12)$$

Differently from the unidirectional case, the counter-densities (in direction j) now parametrize both sending and receiving flow, and through this the transmitted flow.

By construction, one has

$$\text{FD}(\varrho \mid \varrho') = Q(\varrho, \varrho \mid \varrho', \varrho') \quad (13)$$

$$= \min\{S(\varrho \mid \varrho'), R(\varrho \mid \varrho')\}, \quad (14)$$

meaning that if both sides of the interface carry the same density configuration $(\varrho_{i,l}, \varrho_{j,l}) = (\varrho_{i,r}, \varrho_{j,r}) = (\varrho, \varrho')$, then the flow across the interface is identical to the flow within the link on either side of the interface and given by the fundamental diagram (4a)-(4c).

For zero counter-densities, one obtains

$$Q(\varrho, \varrho \mid 0, 0) = \min\{S(\varrho \mid 0), R(\varrho \mid 0)\} \quad (15)$$

$$= \min\{\hat{v}\varrho, w(\hat{\varrho} - \varrho)\}, \quad (16)$$

meaning that the bidirectional model falls back to the unidirectional case considered by Daganzo (1994) for a triangular fundamental diagram.

Another relevant property is related to the microscopic process of particles approaching the interface from one side and exchanging positions with particles approaching it from the opposite side, even when the sum of densities on either side of the interface equals jam density. Discussions of this phenomenon can be found in Wang and Chen (2009), Zhang (2012) and Fu et al. (2013). The interface model (12) allows for such swapping flows. To exemplify this, consider the case $\varrho_{l,i} = \varrho_{r,i} = \varrho_{l,j} = \varrho_{r,j} = \hat{\varrho}/2$. Summing over both directions, jam density is attained both left and right of the interface. Still, (12) predicts a flow of $w\hat{\varrho}/2$ in either direction, meaning that jam density is maintained and all flow movement may be interpreted as swapping.

It now is possible to justify the concrete choice of critical flow $\varrho^*(\varrho') = w\hat{\varrho}/2$ for counter-densities $\varrho' \geq \hat{\varrho}/2$ in (7b). As the counter-density ϱ' is increased from zero up to $\hat{\varrho}/2$, the critical flow falls strictly monotonously down to $w\hat{\varrho}/2$, cf. (7a). This downward monotonicity is plausible because the counter-density hinders the flow. A further increase of ϱ' should hence maintain this monotonicity. Still, an increased counter-density also provides swapping opportunities. As discussed in Flötteröd and Lämmel (2015, Sec. 2.5), $w\hat{\varrho}/2$ is the largest flow that can be transferred across an interface by swapping only. The interface model hence merely abstains from introducing additional constraints and keeps the flow capacity at this level for all $\varrho' \geq \hat{\varrho}/2$.

It is not self-evident that inserting the interface model (12) into a space- and time-discrete numerical scheme keeps densities from eventually exceeding jam density, given that such a constraint is not explicitly enforced. The following result ascertains this property.

Proposition 1. Consider Fig. 4 with cells of length Δx left and right of the interface. Assign to both cells identical \hat{v} , $\hat{\varrho}$, D parameters and discretize time into intervals of length Δt with $\hat{v} \leq \Delta x/\Delta t$. Consider any configuration of non-negative densities $\varrho_{i,l}, \varrho_{j,l}, \varrho_{i,r}, \varrho_{j,r}$ respecting (1). Transmitting constant flows $q_i = Q(\varrho_{i,l}, \varrho_{i,r} \mid \varrho_{j,l}, \varrho_{j,r})$ and $q_j = Q(\varrho_{j,r}, \varrho_{j,l} \mid \varrho_{i,r}, \varrho_{i,l})$ for a duration of Δt time units does not exceed the jam density $\hat{\varrho}$ in either cell.

Proof. Provided in Appendix B. \square

Finally, it needs to be emphasized that this is a continuum model assuming that opposite flows mix perfectly when moving through each other. This does not accommodate an explicit representation of lane formation. The sole modeling degree of freedom for controlling the friction between opposite flows is the conflict delay parameter D .

4.2. Simulation studies with the linear interface model

The following presents simulation (i.e. numerical evaluation) results of the flow exchanged across an interface, using the model (12).

4.2.1. Flow regimes

Using the notation of Fig. 4, the densities $\varrho_{j,l}$, $\varrho_{j,r}$ and $\varrho_{i,r}$ are set to constant values, always with $\varrho_{j,l} = 0$, and the density $\varrho_{i,l}$ is varied in the interval $[0, \hat{\varrho}]$. Fig. 5 displays four configurations. Each plot display flows over $\varrho_{i,l}$ values, using the parameters $\hat{v} = 1.0$ m/s, $\hat{\varrho} = 5$ ped/m and $D = 0.5$ s. In the first diagram, the right-hand side of the interface is empty; in the remaining diagrams it is filled up to jam density in three different configurations. The following results are obtained.

- The first plot shows results for $\varrho_{i,r} = 0$ and $\varrho_{j,r} = 0$. With no pedestrians on the right, flow can only come from the left and $q_j = 0$. As $\varrho_{i,l}$ increases, the flow q_i grows linearly until it reaches the flow capacity $\varrho^*(0)$. This unidirectional example effectively plots the sending function $S(\varrho_{i,l} \mid 0)$ over $\varrho_{i,l}$.
- The second plot shows results for $\varrho_{i,r} = 0.3\hat{\varrho}$ and $\varrho_{j,r} = 0.7\hat{\varrho}$, summing up to $\varrho_{i,r} + \varrho_{j,r} = \hat{\varrho}$. As $\varrho_{i,l}$ is increased, four phases can be observed.
 - First, q_i increases with $\varrho_{i,l}$ as $S_{i,l}$ is the limiting constraint in direction i . The density on the left is not yet large enough to affect the counter-flow q_j , which stays at a constant level.
 - Eventually, q_i reaches the limits of what can be received right of the interface and stays at a constant value of $R_{i,r}$. (The outflow capacity from the left, which can be identified in the first plot, is not reached.) q_j is still not affected.
 - Then, $\varrho_{i,l}$ reaches a magnitude that reduces $R_{j,l}$ to an extent that leads to a decrease in q_j .
 - Finally, $\varrho_{i,l}$ becomes so large that $R_{j,l}$ and hence q_j fall down to the constant value given by (11b). Many pedestrian push now from both sides towards the interface, and all flow exchange can be attributed to swapping (hence $q_i = q_j$).
- The third plot shows results for $\varrho_{i,r} = \varrho_{j,r} = \hat{\varrho}/2$. As before, q_i increases with $\varrho_{i,l}$ until it is limited by $R_{i,r}$. No matter how large $\varrho_{i,l}$ gets, q_j is not reduced: The relatively larger counter-density $\varrho_{i,r}$ right of the interface renders the constant $S_{j,r}$ the dominant constraint on q_j .
- The fourth plot considers $\varrho_{i,r} = 0.7\hat{\varrho}$ and $\varrho_{j,r} = 0.3\hat{\varrho}$. Qualitatively similar curves as in the third plot can be observed, but now at overall lower flow values: q_i is eventually bound by the now relatively low $R_{i,r}$ (a spill-back effect of the relatively large $\varrho_{i,r}$); q_j is constant at $S_{j,r}$.

In the second to fourth configuration, the sum of densities right of the interface equals jam density. Compliance with (1) requires that the amount of flow q_i sent towards the right must not exceed what leaves the right, i.e. q_j . The plots confirm this property.

In summary, it can be stated that the bidirectional sending and receiving flows exhibit plausible interactions and monotonicity behavior, and that a flow exchange is possible even when jam density is reached.

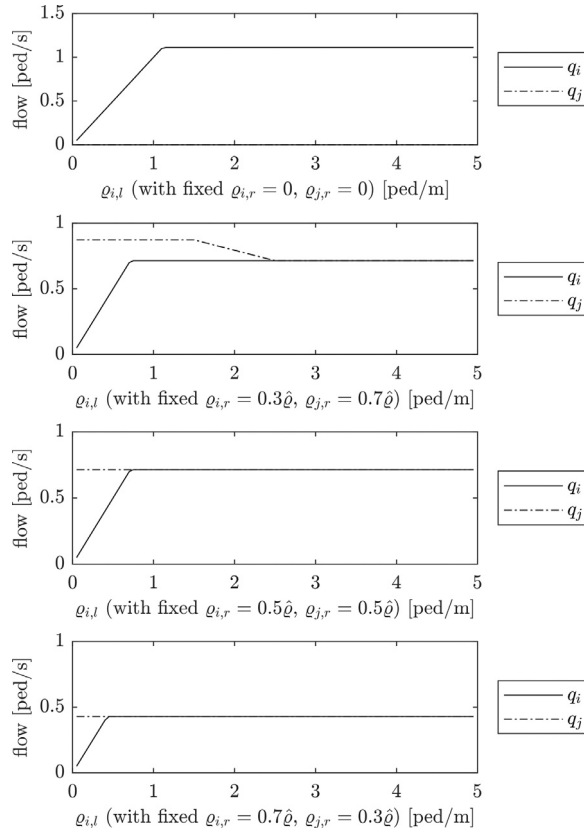


Fig. 5. Flows q_i and q_j as a function of $\varrho_{i,l}$ (with $\varrho_{j,l} = 0$ throughout).

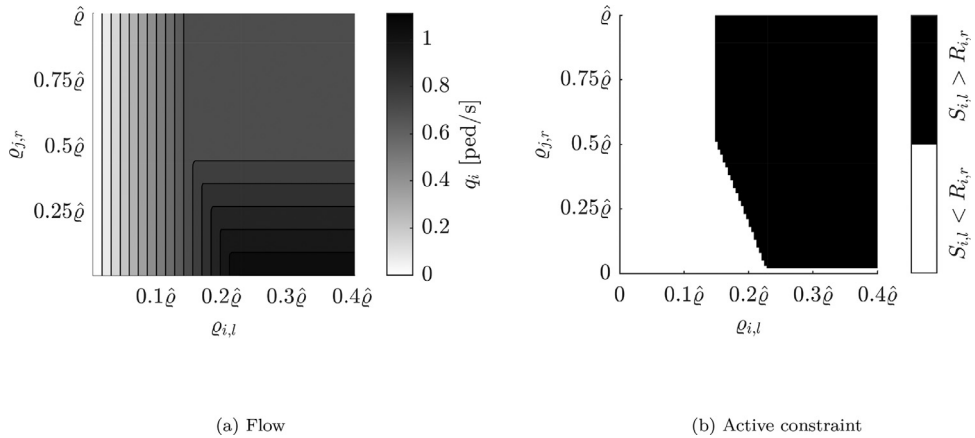


Fig. 6. Flow and active constraint over boundary densities.

4.2.2. Active constraints

The same notation and parameters as before are used, but different densities are considered: The full range of possible $\varrho_{i,l}$ and $\varrho_{j,r}$ values is explored, while the remaining densities are set to zero: $\varrho_{j,l} = \varrho_{i,r} = 0$. This means that only densities moving towards the interface attain non-zero values.

Fig. 6 (left) shows the flow q_i over densities $(\varrho_{i,l}, \varrho_{j,r})$. Direction- i flows beyond $\varrho_{i,l} = 0.4\hat{\varrho}$ are constant and hence not shown. The direction- j flow is omitted, as it is symmetric to q_i . For any given counter-density $\varrho_{j,r}$ the direction- i flow q_i grows linearly with $\varrho_{i,l}$ until it reaches $R_{i,r} = R(0 \mid \varrho_{j,r})$. This receiving function, in turn, falls from $q^*(0)$ at $\varrho_{j,r} = 0$ to $w\hat{\varrho}/2$ at $\varrho_{j,r} = \hat{\varrho}/2$, at which level it stays for larger values of $\varrho_{j,r}$. Overall, q_i grows (not strictly) monotonously with $\varrho_{i,l}$ and falls (not strictly) monotonously with $\varrho_{j,r}$. For high densities on both sides of the interface, a constant and strictly positive flow

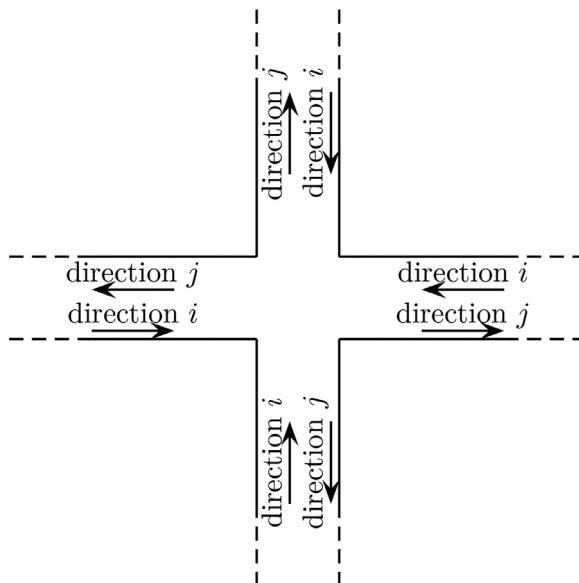


Fig. 7. Node Intersection.

$q_i = q_j = w\hat{\rho}/2$ arises; this can be interpreted as a situation where two pedestrian groups moving in opposite directions meet and push through each other by swapping.

Fig. 6 (right) indicates if the direction- i flow is sending- or receiving-constrained. Apart from what has already been said when discussing the flow q_i itself, it can be noted that the density $\rho_{i,l}$ at which the direction- i flow switches from under- to over-critical (i.e. from sending to receiving) becomes the smaller the larger the counter-density $\rho_{j,r}$ is.

5. General intersection model

The linear interface model is now generalized to intersections of more than two links, as illustrated in Fig. 7. In a unidirectional flow model, each of the four approaches would only be allowed to either carry a node inflow (upstream link) or a node outflow (downstream link). In the considered bidirectional case, flows in both directions are jointly present in each link.

The following notation is used. A node is the intersection of N links, which are indexed by $m, n = 1, \dots, N$. Where up- and downstream links need to be distinguished, m is used to index upstream links and n refers to downstream links. On each link, the flow into the node is indexed by i , and the flow out of the node is indexed by j . This deviates somewhat from the convention used for a linear interface, where direction i (resp. j) was “left to right” (resp. “right to left”) in both links. This simplified the presentation but is not applicable to a general intersection, where the notions of “left” and “right” are not well defined.

The flow from link m into the node is $q_{i,m}$, and the flow out of the node into link n is $q_{j,n}$; densities are indexed accordingly. The share of link m 's outflow that enters link n is p_{mn} . Flows are conserved within the node.

5.1. The Incremental Node Model

Flötteröd and Rohde (2011) propose a continuum flow node model for road traffic intersections. The model is compatible with unidirectional KWM link flow dynamics. It is called Incremental Node Model (INM) because it incrementally transmits flows across the intersection until the following set of constraints does not allow for a further flow increase:

- The flow leaving an upstream (of the node) link must not be larger than that link's sending flow.
- The flow entering a downstream (of the node) link must not be larger than that link's receiving flow.
- Flow leaving an upstream link m is distributed towards downstream links n according to exogenously given turning fractions.
- A priority rule defines how a limited receiving flow is distributed across competing sending flows.

The unidirectional INM for a node with $m = 1, \dots, N$ ingoing and $n = 1, \dots, N$ outgoing links is recalled in Algorithm 1. Underlined statements in the algorithm refer to the yet to be introduced bidirectional extension of the INM and may be ignored for the time being. The “ \leftarrow ” operator represents an assignment from right to left; in cases where the same variable appears on both sides, the right-hand side is evaluated before it is assigned to the left-hand side.

Algorithm 1 Bidirectional Incremental Node Model (INM).

1. Given:

(a) Physical model parameters: \hat{v} , w , \hat{Q} , $P = (p_{mn})$ and, if bidirectional, D , respecting (3).(b) Boundary conditions: Inflow densities $Q_{i,m}$, outflow densities $Q_{j,n}$.2. Initialize sending flows $\mathbf{S} = (S_m)$, receiving flows $\mathbf{R} = (R_n)$, node inflows $\mathbf{q} = (q_m)$ and, if bidirectional, $\mathbf{K} = (K_n)$:

$$S_m \leftarrow S(Q_{i,m} \mid Q_{j,m}) \quad (22)$$

$$R_n \leftarrow R(Q_{j,n} \mid Q_{i,n}) \quad (23)$$

$$q_m \leftarrow 0 \quad (24)$$

$$\text{If bidirectional: } K_n \leftarrow w(\hat{Q} - Q_{i,n} - Q_{j,n}) \quad (25)$$

3. Repeat:

(a) Compute transmission rates and adjust if bidirectional:

$$\varphi_m \leftarrow \begin{cases} 1 & \text{if } S_m - q_m > 0 \text{ and } \forall n : (R_n - \mathbf{p}_n^T \mathbf{q} > 0 \text{ or } p_{mn} = 0) \\ 0 & \text{otherwise} \end{cases} \quad (26)$$

$$\text{If bidirectional: } \varphi \leftarrow \operatorname{argmin}_{\mathbf{x}=(x_m)} \sum_m (x_m - \varphi_m)^2 \text{ s.t. } \begin{cases} \mathbf{x} \in [\mathbf{0}, \varphi] \\ (P^T - I)\mathbf{x} \leq \mathbf{K} - (P^T - I)\mathbf{q} \end{cases} \quad (27)$$

(b) if $\varphi = \mathbf{0}$: RETURN node inflows \mathbf{q} and TERMINATE.

(c) Compute transmission factor and update node inflows:

$$\theta \leftarrow \operatorname{argmax}_{t \in \mathbb{R}} t \text{ s.t. } \begin{cases} t\varphi \leq \mathbf{S} - \mathbf{q} \\ P^T(t\varphi) \leq \mathbf{R} - P^T \mathbf{q} \\ \text{If bidirectional: } (P^T - I)(t\varphi) \leq \mathbf{K} - (P^T - I)\mathbf{q} \end{cases} \quad (28)$$

$$\mathbf{q} \leftarrow \mathbf{q} + \theta\varphi. \quad (29)$$

The algorithm takes in Step 1 physical model parameters and adjacent link densities as inputs. In the unidirectional case, node inflow densities are zero in downstream links n and node outflow densities are zero in upstream links m . The turning fractions towards link n are stacked in a vector \mathbf{p}_n , and all of these vectors are then combined into the turning fraction matrix $P = (p_{mn})$ as follows:

$$\mathbf{p}_n^T = (p_{1n} \cdots p_{Nn}) \quad (17)$$

$$P = (\mathbf{p}_1 \cdots \mathbf{p}_N) \quad (18)$$

with superscript T denoting the transpose.

The following vectorial representations of sending flows \mathbf{S} and node inflows \mathbf{q} (containing one entry S_m resp. q_m per node upstream link) and of receiving flows \mathbf{R} (containing one entry R_n per node downstream link) are used:

$$\mathbf{S} = (S_{i,1} \cdots S_{i,m} \cdots S_{i,N})^T \quad (19)$$

$$\mathbf{R} = (R_{j,1} \cdots R_{j,n} \cdots R_{j,N})^T \quad (20)$$

$$\mathbf{q} = (q_{i,1} \cdots q_{i,m} \cdots q_{i,N})^T \quad (21)$$

These variables are initialized in Step 2, where the unidirectional case is captured by using zero counter-densities, meaning that (22) and (23) evaluate $S(\cdot \mid 0)$ resp. $R(\cdot \mid 0)$.

Now, the algorithm runs through a finite number of iterations. During these iterations, it incrementally computes flow transmissions according to the following logic.

Step 3a assigns in (26) a transmission rate φ_m to each upstream link m . In the vehicular case, this rate can be interpreted as a priority in that a larger value gives higher precedence when competing for limited space in a downstream link. In the pedestrian case, all links are given the same priority. The transmission rate is hence set to one for all upstream links that can at all send more flow. For this, two conditions need to be satisfied: (i) The sending flow S_m of the considered link m is not yet exhausted, i.e. smaller than the so far transmitted flow q_m , and (ii) the receiving flow R_n of all downstream links n towards which the considered link m has a nonzero turning fraction p_{mn} is not yet exhausted, i.e. smaller than the so far received flow, which is given by $\mathbf{p}_n^T \mathbf{q}$.

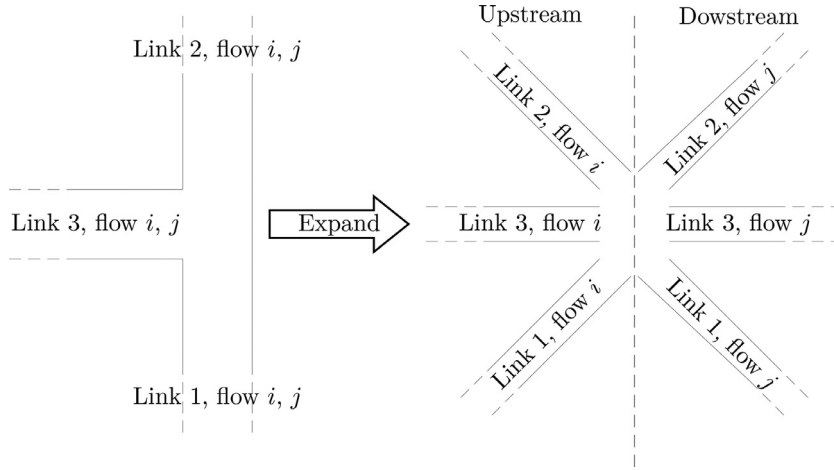


Fig. 8. Unidirectional expansion of a bidirectional node.

If all transmission rates are zero, meaning that no upstream link can send more flow, Step 3b terminates the algorithm and reports the node inflows \mathbf{q} as the model's solution.

Otherwise, Step 3c transmits further flow from all upstream links proportionally to their transmission rates. For this, the largest multiple θ of the transmission rate vector $\boldsymbol{\varphi} = (\varphi_m)$ that can be transmitted without violating a sending or receiving flow constraint is identified in (28). The resulting flow increment is then added to the inflow vector \mathbf{q} in (29).

5.2. Representation of a bidirectional node in the INM

In order to solve a bidirectional flow problem with the INM, all bidirectional links are decomposed into two unidirectional links, one carrying the direction- i flow into the node and one carrying the direction- j flow out of the node. Fig. 8 provides an illustration. The flows across the expanded node can be computed using the unidirectional INM, with the sending flows of all upstream links being given by $S_{i,m} = S(\varrho_{i,m} | \varrho_{j,m})$ and the receiving flows of all downstream links being given by $R_{j,n} = R(\varrho_{j,n} | \varrho_{i,n})$. The underlined items in Algorithm 1 are still not needed to (naively) evaluate the INM on the expanded node.

5.3. Compliance with the jam density constraint (1)

Without further precaution, an application of the INM to the expanded unidirectional version of a bidirectional node may lead to violations of the upper (jam) density constraint (1). This is illustrated in the bidirectional three-leg intersection of Fig. 9. All flow from link 1 goes to link 2 and all flow from link 2 goes to link 3, i.e. $p_{12} = p_{23} = 1$. Links 1 and 2 are ready to send flow into the node ($S_{i,1}, S_{i,2} > 0$). Link 3 spills back: $\varrho_{j,3} = \hat{\varrho}$, meaning that the link is filled with pedestrians aiming to move away from the node, which implies $R_{j,3} = 0$ by (11c). Also link 2 has reached jam density, but with a bidirectional mix of densities: $\varrho_{i,2} = \varrho_{j,2} = \hat{\varrho}/2$, implying $R_{j,2} > 0$ from (11b). The (naive) INM would in this setting compute a zero flow from link 2 (because the receiving flow of link 3 towards which 2 wants to send is zero) but a strictly positive flow from 1 into 2 (because 1 has a strictly positive sending flow only towards 2, and 2 has a strictly positive receiving flow). This means that the density on link 2 would increase beyond jam density. Proposition 1 does not apply in this case; it only considers a linear interface.

In a spatiotemporally discrete setting where constant flow rates are transmitted in time intervals of duration Δt between cells of length Δx with $\hat{v} \leq \Delta x / \Delta t$, the following condition implies compliance with the jam density constraint (1) on link n :

$$q_{j,n} - q_{i,n} \leq w(\hat{\varrho} - \varrho_{i,n} - \varrho_{j,n}) \quad (30)$$

with $q_{j,n}$ being the flow from the node into the link and $q_{i,n}$ being the flow out of the link towards the node. Multiplying both sides of this expression by Δt turns its l.h.s. into the effective amount of flow entering link n (inflow minus outflow), and its r.h.s. into at most the amount of available space in that link. The latter fact is a result of $w \leq \hat{v}$ following from (3), which implies $w\Delta t \leq \hat{v}\Delta t \leq \Delta x$. Letting

$$K_n = w(\hat{\varrho} - \varrho_{i,n} - \varrho_{j,n}) \quad (31)$$

$$\mathbf{K} = (K_n), \quad (32)$$

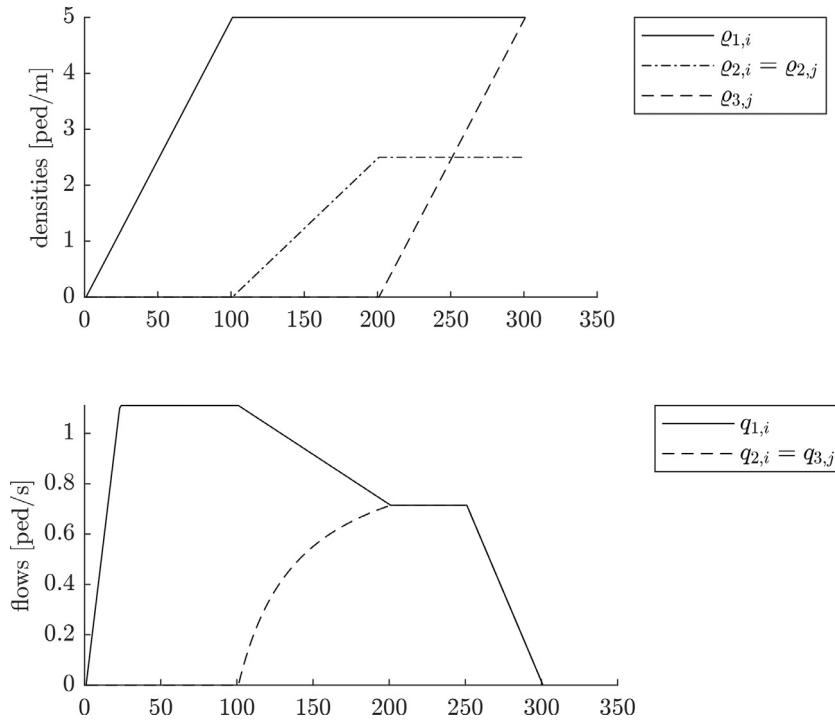


Fig. 10. Illustration of bidirectional INM.

Corthout et al. (2012) for capturing within-node conflicts in the vehicular case may carry over to the pedestrian setting considered here.

5.4. Simulation study with the bidirectional INM

The three-leg intersection shown in Fig. 9 and described in Section 5.3 is considered. Recall that all flow from link 1 goes into link 2 and all flow from link 2 goes into link 3. The behavior of the bidirectional INM is illustrated by gradually changing the node boundary densities and observing the resulting node inflows. The model is parametrized with $\hat{v} = 1$ m/s, $\hat{\varrho} = 5$ ped/m, $D = 0.5$ s. Fig. 10 displays the chosen node boundary densities resp. resulting inflows in the first resp. second row. Both subfigures display physical quantities over an otherwise irrelevant time-line along which densities are varied. At each point along this time line, the given boundary densities (upper subfigure) are fed into Algorithm 1, the algorithm is run to termination, and the resulting flows (lower subfigure) are observed. All densities are initially zero.

During the first 100 time steps, the inflow density $\varrho_{1,i}$ of link 1 is increased from zero to jam density $\hat{\varrho}$. This is an effectively unidirectional setting, in which the outflow $q_{1,i}$ of link 1 increases linearly until it reaches the unidirectional flow capacity, at which it then stays.

Keeping $\varrho_{1,i}$ at $\hat{\varrho}$, the in- and outgoing densities $\varrho_{2,i}$ and $\varrho_{2,j}$ of link 2 are during time steps 100 to 200 jointly increased from zero to $\hat{\varrho}/2$ each. Given that the sending flow of link 1 is at capacity, the resulting decrease of $q_{1,i}$ is attributed to a reduced receiving flow of link 2. The linear shape of this decrease can be explained in terms of Fig. 2(b): Jointly increasing both densities on link 2 corresponds to moving away from the origin along the main diagonal of this figure, along which path the receiving function falls linearly. The decreasing pace at which the flow $q_{2,i}$ from link 2 grows can be attributed to the corresponding shape of the sending function along the main diagonal of Fig. 2(a). As the total density in link 2 approaches jam density in time step 200, the flow that is allowed to enter link 2 (from link 1) is constrained to the amount that simultaneously leaves link 2.

Keeping $\varrho_{1,i}$ at $\hat{\varrho}$ and $\varrho_{2,i} = \varrho_{2,j}$ at $\hat{\varrho}/2$, the node outflow density $\varrho_{3,j}$ on link 3 is between time steps 200 and 300 increased from zero to $\hat{\varrho}$. As long as $\varrho_{3,j}$ is relatively low, it does not impede the flow entering link 3 from link 2. Eventually, link 3's receiving flow starts falling linearly towards zero, which induces a corresponding node inflow decrease from link 2; this can be interpreted as a spill-back of pedestrians from link 3 into link 2. As the flow from link 2, which is at jam density, decreases, less space becomes available for pedestrians approaching link 2 from link 1, hence also reducing link 1's flow into the node. Once the outflow density on link 3 reaches jam density, all flows cease: All links are at jam density, and there is no swapping flow possible between links 1 and 2 because the flow from link 2 is blocked by the spill-back from link 3.

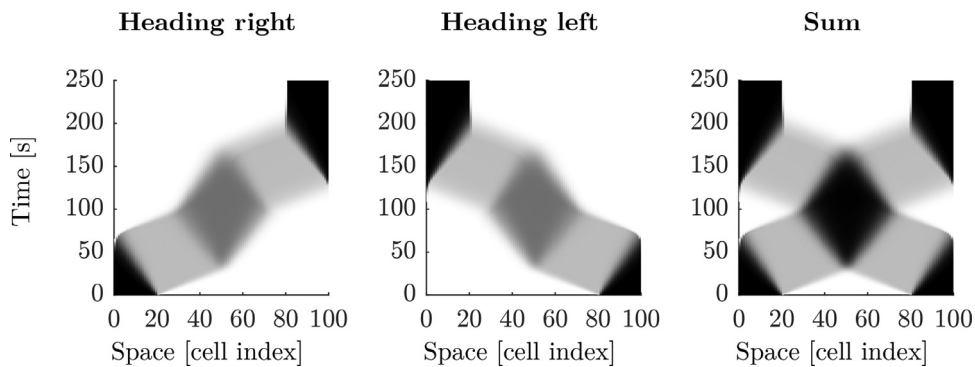


Fig. 11. Space/time density plots in linear corridor (white=zero density, black=jam density).

6. Simulation studies with a bidirectional network cell-transmission model

This section presents simulation results that are obtained by inserting the proposed node model into a cell-based pedestrian network discretization. The result is a bidirectional cell-transmission model (CTM). Following illustrative experiments in synthetic settings, a first comparison to a real dataset is presented.

A CTM network discretization is obtained as follows. A time step length $\Delta t > 0$ is chosen. All network links are discretized into cells of length $\Delta x \geq 2\hat{v}\Delta t$. The lower bound is chosen twice as large as in the unidirectional case because the bidirectional model allows for waves traveling at \hat{v} towards each other.

Flow transmissions between the cells within a link are evaluated using (12); flows across nodes where more than two links meet are described by the general INM of Algorithm 1. (As explained in Section 5.3, (12) and Algorithm 1 yield identical results within a channel.)

After initializing the network with two direction-dependent density values in each cell, the following sequence of computations evaluates the CTM in a time-stepping manner:

1. Given the densities in all cells, compute sending and receiving flows at all cell interfaces.
2. Given the sending and receiving flows, compute flow transmissions across all cell interfaces.
3. Given the flow transmissions, update densities in all cells such that pedestrian mass is conserved.

This overall structure is the same as in the broadly known unidirectional CTM. The relevant difference is that in the bidirectional case each cell carries two direction-specific densities, which the cell sends/receives in opposite directions.

Three synthetic and one real scenario are subsequently presented. All use the parameters $\hat{v} = 1$ m/s, $\hat{q} = 5$ ped/m, a time step length of $\Delta t = 0.5$ s and a cell length of $\Delta x = 1$ m. The synthetic scenarios use $D = 0.5$ s; the real scenario is evaluated with a range of D values.

The first synthetic scenario considers a linear corridor, the second and third scenario consider three links interacting through one intersection node in different configurations. All synthetic scenarios consider a closed system (no flow enters or leaves the system) and use as boundary condition an initial density profile on all cells. The real scenario considers an initially empty three-leg intersection and explicitly models boundary in- and outflows.

6.1. Bidirectional CTM in a linear corridor

This scenario considers a linear corridor divided into 100 equally long cells. The system is initialized by filling the 20 leftmost cells up to jam density with pedestrians heading to the right and the 20 rightmost cells up to jam density with pedestrians heading to the left. The system is evaluated for 250 time steps.

Results are presented in Fig. 11. The two initial density profiles fan out consistently with what a unidirectional KWM would predict. Once the two flows meet in the center of the corridor around time step 25, they slow down while seeping through each other at in total jam density (visible as the diamond-shaped black region in the center of the third subfigure). Pedestrians that have moved through this swapping region return to free-flow speed until they eventually queue up at jam density at the respective end of the corridor (where no flow gets to leave the system); this is again what a unidirectional KWM would predict as well.

6.2. Bidirectional CTM around a three-legged intersection

An intersection connecting three bidirectional links is considered, cf. Fig. 12. All links are discretized into 100 cells, with increasing cell indices towards the node. The first 20 (i.e. furthest away from the node) cells of all links are filled up to jam density with pedestrians moving towards the node, all other cells are initially empty. The system is evaluated for two different turning fraction matrices.

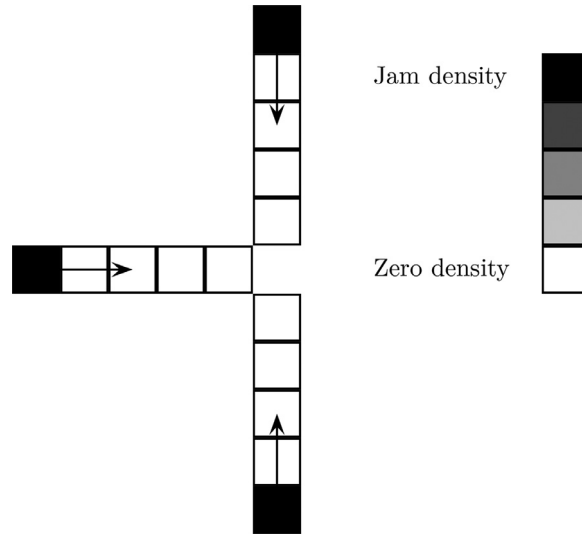


Fig. 12. Three-leg intersection scenario.

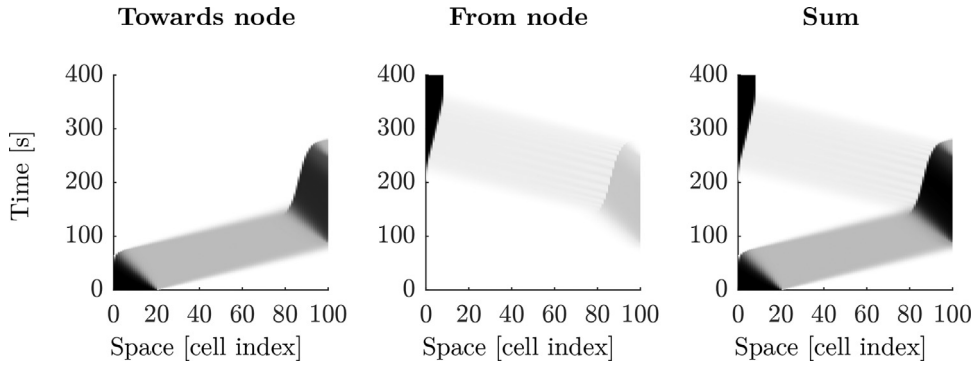


Fig. 13. Space/time density plots with symmetric turning fractions (white=zero density, black=jam density).

These simulation studies also illustrate the possibility of a node “blocking” (i.e. ceasing to transmit flow), and how an adjustment of the INM’s transmission rates can remedy this possibly unwanted effect.

6.2.1. Symmetric turning fractions

This scenario is characterized by the turning fraction matrix

$$P = \begin{pmatrix} 0 & 0.5 & 0.5 \\ 0.5 & 0 & 0.5 \\ 0.5 & 0.5 & 0 \end{pmatrix}, \quad (36)$$

meaning that the flow reaching the node from any link splits uniformly into the two other links. The system is evaluated for in total 400 time steps. Due to the symmetry of this configuration, all three links exhibit identical flow dynamics; Fig. 13 hence shows results for a single link.

The initial density profile fans out and moves at free flow speed towards the node. Eventually, the pedestrians on a given link encounter the first pedestrians coming from the other links. The flows seep through each other at (in sum) jam density. After this, they continue at free flow speed until they have reached the end of their destination link, where they queue up because no flow gets to leave the system. As in the corridor example, the episodes of unidirectional flow are consistent with KWM dynamics.

6.2.2. Non-symmetric turning fractions

The turning fractions considered in this case are

$$P = \begin{pmatrix} 0 & 0.9 & 0.1 \\ 0.2 & 0 & 0.8 \\ 0.2 & 0.8 & 0 \end{pmatrix}. \quad (37)$$

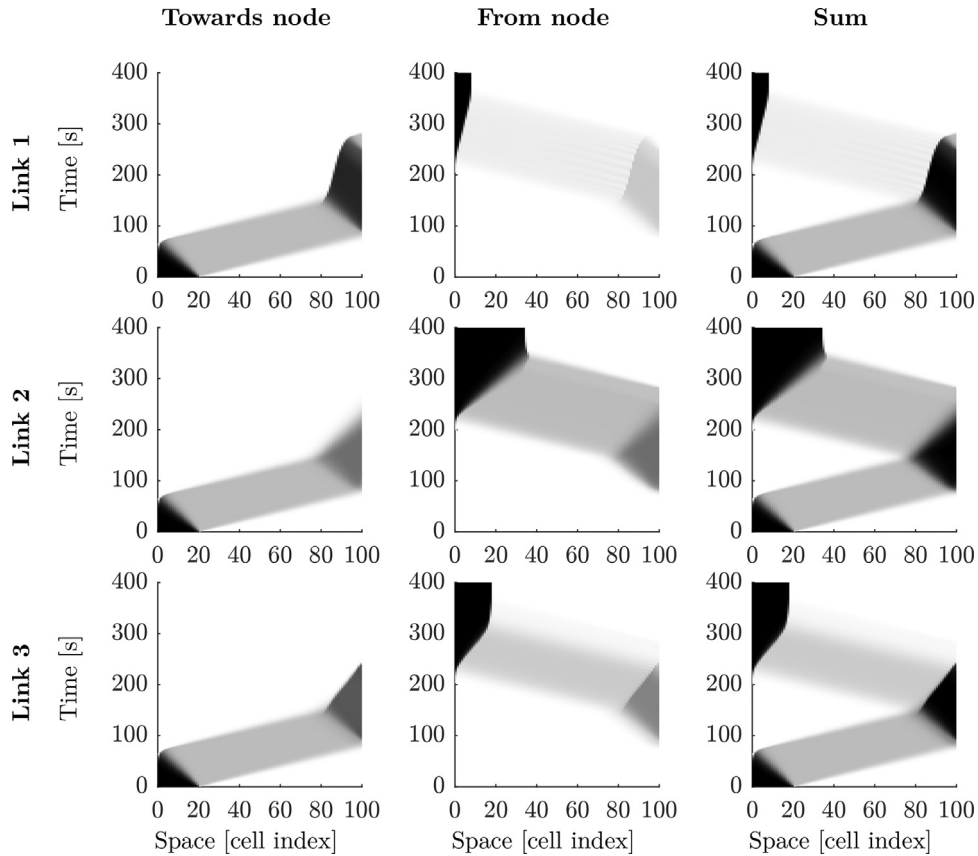


Fig. 14. Space/time density plots with non-symmetric turning fractions (white=zero density, black=jam density).

This means that link 1 sends most of its flow into link 2, link 2 sends most flow to link 3, and link 3 sends most of its flow to link 2. Overall, the largest amount of flow is hence directed into link 2.

Fig. 14 show the results, with one row per link and the columns indicating, as before, densities heading towards the node, away from the node, and their sum. All links exhibit qualitatively similar behaviors, with quantitative differences arising from the non-symmetric turning fractions.

The flows originating in link 1 and 3 compete for being able to enter link 2; their queues towards the node hence take a longer time to dissipate than on link 2. (These queues can be identified as the dark, near-triangular regions around time index 200 and cell index 100 in the first column). Link 1 wants to send a larger fraction (90%) of its flow than link 3 (80%) into link 2, hence the queue on link 1 takes longer to dissipate. After the flows have moved through each other, they move towards the end of their respective destination link, where they again queue up. The sizes of these final queues (in the top left corner of all subfigures in the second column) reflect the amount of flow sent into the respective link. As before, unidirectional episodes are compatible with a KWM, with plausible flow reductions and delays arising where counter-flow is present.

Attention is now focused on the situation where the region of link 2 nearest to the node is filled up to jam density with bidirectional densities; this is visible as the black triangle around cell index 100 and time index 150 in the third subfigure of row 2. The constraint in (35) ensuring that link 2 in this situation does not exceed jam density reads as follows:

$$0.9 \cdot \theta \varphi_1 + 0.8 \cdot \theta \varphi_3 - \theta \varphi_2 \leq 0, \quad (38)$$

where the r.h.s. is zero because it is proportional to the available space in the link, cf. (31). If now (26) in Step 3a of Algorithm 1 computes transmission rates $\varphi_1 = \varphi_2 = \varphi_3 = 1$, any strictly positive transmission factor θ violates this constraint, meaning that (28) in Step 3c yields a zero θ value. Here, the transmission rate adjustment of (27) in Step 3a takes notable effect. A more detailed inspection of the simulation process reveals that the rates φ_1 and φ_3 are reduced such that a strictly positive transmission factor θ becomes feasible and the node eventually clears all flow. As stated before, this adjustment is to be understood as a modeling degree of freedom that may or may not be used, or even modified, depending on what node behavior is desired.

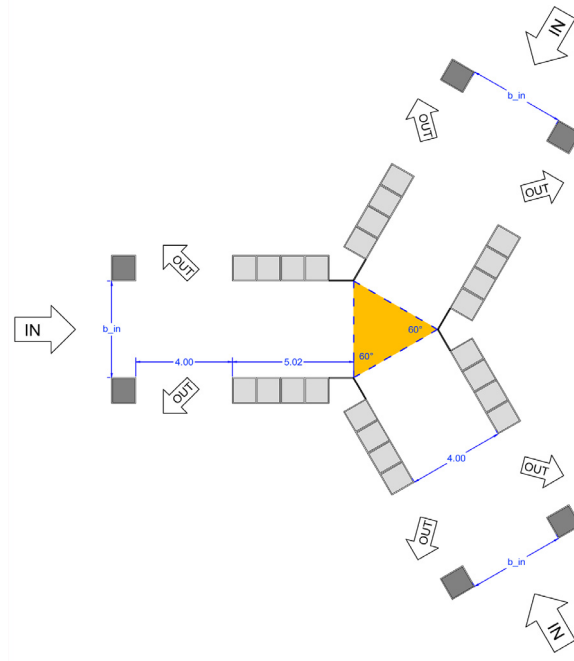


Fig. 15. Jülich experiment, reproduced with permission of S. Holl.

6.2.3. Comparison to a real dataset

The following study demonstrates the model's ability to approximate a real dataset, including the encoding of differently wide channels. The data collection is described in Chapter 3 of [Holl, \(2016\)](#)

Fig. 15 displays the considered symmetric three-leg intersection. Trajectory data and detailed documentation are available under the DOI [10.34735/ped.2013.3](https://doi.org/10.34735/ped.2013.3). The “passes” 2–6 of the experimental series “A” are considered; the first pass of this series is excluded because it uses a systematically different configuration.

Pedestrians enter the intersection straight-on from all approaches. They are given directional instructions such that the flow from each approach splits approximately uniformly into the two other channels. Pedestrians leave the channel leading them away from the node to the side. The passes differ only in their (in-)flow levels, which are controlled by setting the width b_{in} of the entry gates. The number of participants in the experiment is large enough to ensure that the entry gate width rather than a possible lack of pedestrians available for entering limits the inflow. The fixed channel width near the central node is 4 meters, the length of each channel is between 9.02 meters when excluding the triangular central node and 10.17 meters when measuring all the way to the node's center point.

Modeling the variable entry gate width requires interfacing differently wide cells (resp. channels). This can be formulated in different ways; the following presentation adheres as much as possible to the so far adopted linear channel representation. The physical width b_{phys} of a cell is translated into a unit-less multiple b_{rel} of a single pedestrian's width b_{ped} :

$$b_{rel} = \frac{b_{phys}}{b_{ped}}. \quad (39)$$

With Δx the cell length and c the (direction-specific) number of pedestrians in the cell, the *width-normalized density* \tilde{q} is defined per length unit and per (unit-less) width unit:¹

$$\tilde{q} = \frac{c}{b_{rel} \Delta x}. \quad (40)$$

The width-normalized density can be thought of as representing a b_{ped} wide slice of the cell. Inserting width-normalized densities into the sending and receiving flow functions hence yields the sending and receiving flows of a b_{ped} wide cell slice, which need to be rescaled to match the physical cell dimensions:

$$S = b_{rel} \cdot S(\tilde{q} | \tilde{q}') \quad (41)$$

¹ Not normalizing with b_{rel} does not simplify the formulation because it requires to make the conflict delay parameter dependent on the cell width. This fact can be read out of, e.g., (3), where scaling the jam density with the cell width unjustifiably changes the longitudinal backward wave speed unless one also scales the conflict delay parameter anti-proportionally with that density.

$$R = b_{\text{rel}} \cdot R(\tilde{q} | \tilde{q}') \quad (42)$$

with q' being the width-normalized counter-density. Processing these flows in the interface model (12) or the INM yields flow rates that match the physical cell widths. The total number of pedestrians Δc transmitted at flow rate q during Δt time units is $\Delta c = q\Delta t$. The resulting width-normalized density change is hence

$$\Delta \tilde{q} = \frac{q\Delta t}{b_{\text{rel}}\Delta x}. \quad (43)$$

The scalings with b_{rel} cancel out within a homogeneous channel, where adjacent cells have the same cell width; this can be seen by inserting (cell- and direction-specific versions of) (41), (42) into (12) and combining the result with (43). When interfacing differently wide channels, however, b_{rel} becomes cell-specific and does not cancel out.

The simulation scenario is constructed similarly to what is shown in Fig. 12; each approach is composed of 10 cells of 1 meter length each. The bidirectional INM representing the central node uses symmetric turning fractions, just as shown in (36). The system boundaries are modeled by adding one INM to the peripheral end of each approach. Each such INM is connected to one additional entry and one exit cell, which differ from the within-channel cells only in the following regards: The densities in the exit cells are set to zero throughout the simulation, meaning that there is no spill-back from outside of the system. Each entry cell is as wide as the entry gate. In every simulation time step, it is filled (up to jam density) with pedestrians waiting to enter the approach. In the real experiment, the entry gates are eventually closed such that the system clears; the closing times, which are not exactly available, differ across passes and even across approaches.² This cannot be represented in the model, where the number of pedestrians available to enter the system from each approach is set to one third of all pedestrians having entered the system in the corresponding pass and leaving the gates open throughout.

Each row in Figs. 16 and 17 corresponds to one pass, using a different entry gate width b_{in} . Note the different scalings of the ordinates. The left column shows real inflow rates from all three approaches into the triangular node area shown in Fig. 15, obtained by counting node entries per five-second interval. The right column presents the corresponding simulated flows. By symmetry of the model set-up, the flows in all three approaches are identical. The different curves are obtained using different conflict delay parameters $D = 0.5 \text{ s}, 1.0 \text{ s}, 1.5 \text{ s}, 2.0 \text{ s}$ with otherwise fixed values for $\hat{v} = 1 \text{ m/s}$, $\hat{q} = 5 \text{ ped/m}$, and $b_{\text{ped}} = 0.61 \text{ m}$ (following Fruin et al., 1971, p.67). The model is simulated at 0.5 s time steps.

The real inflow curves (left columns) exhibit, overall, a noisy and roughly rectangular shape. As the inflow gate width increases, the realized node inflows increase only mildly; this can be attributed to the presence of counter-flows. For larger entry gates, one observes in Fig. 17 an initial inflow peak in all approaches. It can be explained by the physical extent of the central node, where it takes a while until the flow-reducing effect of conflicts arising within the node propagate back into the approaches. Some approaches also exhibit flow peaks shortly before the system clears. This is a result of the approaches running empty at different times, meaning that the last pedestrians in the system are less obstructed by counter-flows.

The simulated inflow curves (right columns) are obtained by measuring the center-bound inflow into the cell nearest to the central INM. Given the cell length of one meter, this approximates the inflow to the triangular central region, which separates the approaches by 1.15 m from the triangle's center point. One still recognizes overall rectangular, now smeared-out, flow profiles. The higher the conflict delay parameter D , the more friction arises in the system, resulting in lower flow rates and longer clearance times. The model captures the appearance of an initial inflow peak, cf. Fig. 17. Just like in the real data, this peak is absent or at least less distinct in the experiments with narrower entry gates, cf. Fig. 16. For lower entry gate widths and smaller conflict delay parameters, one observes a second simulated flow peak, which arises as follows. The initial system inflows proceed unhindered to the central INM, where they encounter each other. The resulting flow drop propagates away from the central node into the approaches, creating the downward flank of the first flow peak. It follows a phase during which the flow and density profiles in all channels approach stationarity. For sufficiently narrow entry gates and small conflict delays, the stationary flows are higher than what is observed just before the initially unidirectional approach flows collide with each other. This increase forms the upward flank of the second peak, which falls again as the system clears.

A more precise calibration of this scenario is not attempted; a major obstacle are the in detail unknown gate opening and closing times. One may note that a conflict delay parameter of $D = 1.5 \text{ s}$ yields simulated flows that are in terms of flow levels and durations, as well as overall flow profile shapes near the real data. Even without detailed calibration and validation, it can safely be concluded that the model is structurally capable of capturing bidirectional spatiotemporal flow dynamics in non-trivial channel configurations.

7. Summary

This article formulates a model for bidirectional pedestrian flows across linear and multi-leg intersections. The model rests on the development of bidirectional sending and receiving functions, which are compatible with the bidirectional fundamental diagram of Flötteröd and Lämmel (2015). It is demonstrated how spatiotemporal bidirectional flows on pedestrian

² The available trajectory data does not extend to the gate region, neither does the supplementary video footage cover all gates.

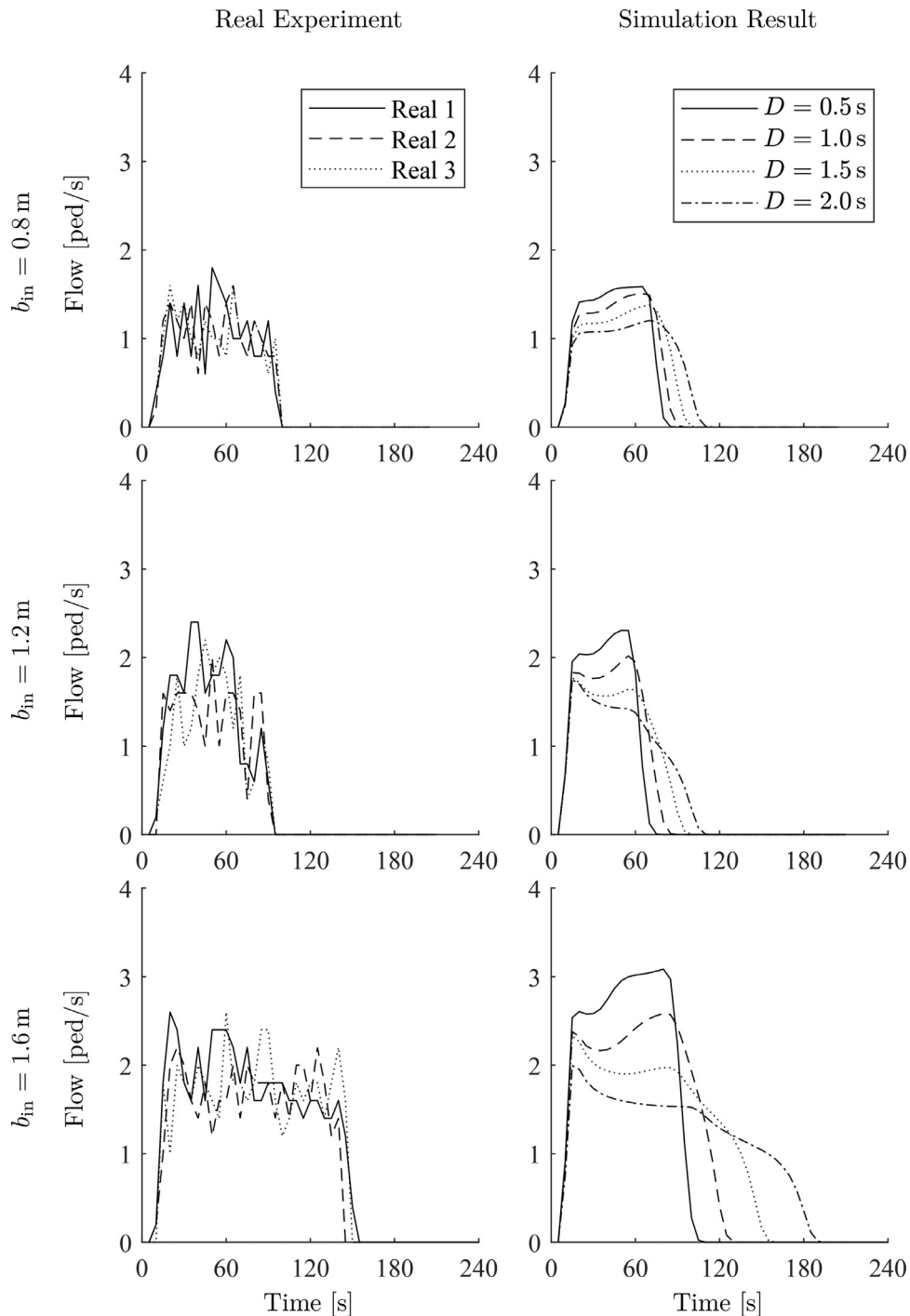


Fig. 16. Jülich experiment, node inflows for narrow entry gates.

networks can be simulated by inserting these sending and receiving functions into a bidirectional cell-transmission model and adopting the incremental node model of Flötteröd and Rohde (2011) to represent multidirectional pedestrian intersections. The model is illustrated through several synthetic simulation experiments and configured to qualitatively reproduce a real dataset.

The model relies on few parameters, which can be interpreted as bidirectional counterparts of the parameters used in a unidirectional kinematic wave model with a triangular fundamental diagram: speed limit, jam density, conflict delay (translating into a backward wave speed) for the dynamics on a linear link, turning fractions to distribute flows across multiple

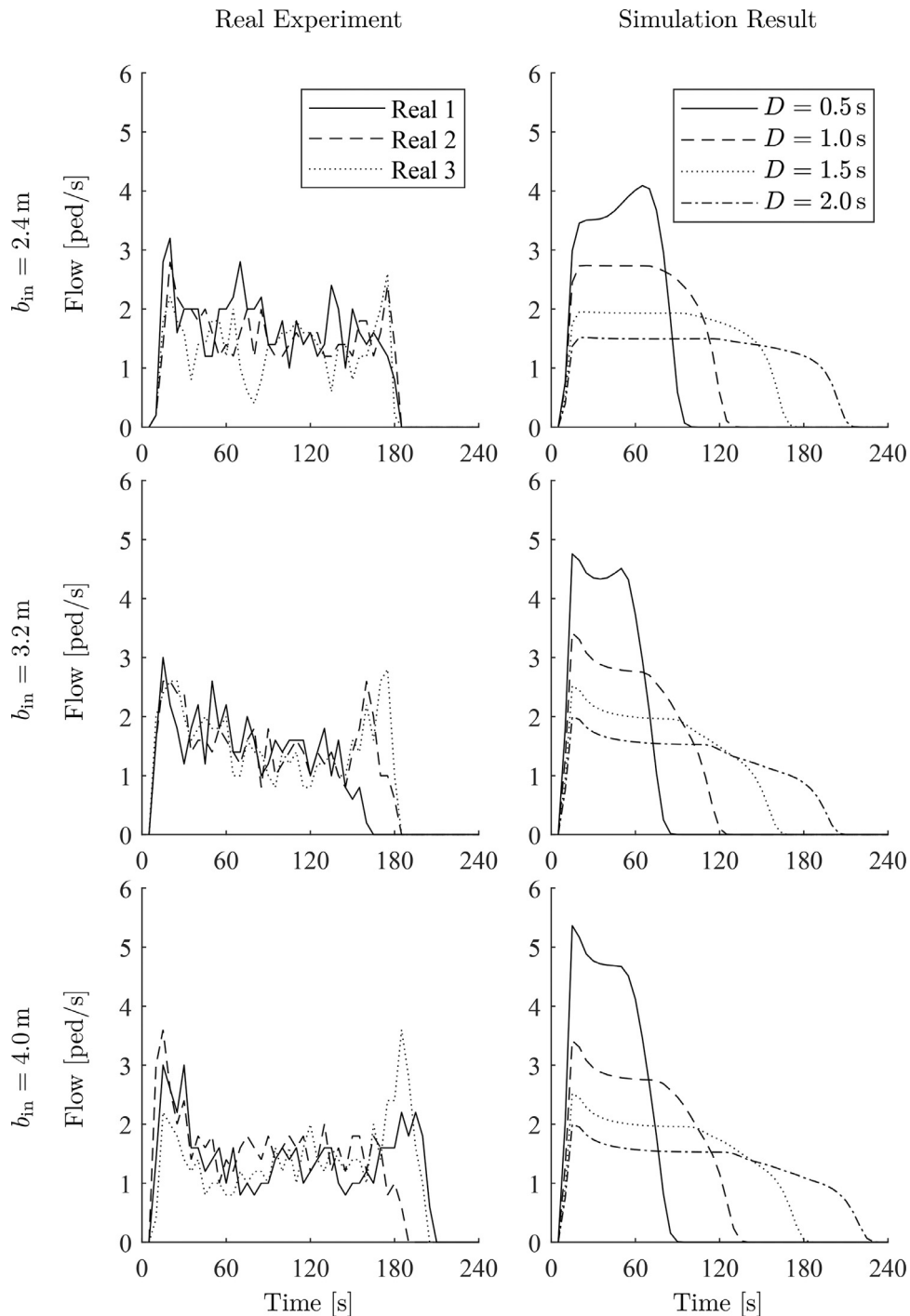


Fig. 17. Jülich experiment, node inflows for wide entry gates.

downstream links. The model is compatible with the KWM where such comparisons are meaningful (i.e. in unidirectional flow episodes), the bidirectional additions yield plausible spatiotemporal dynamics (flows decreasing and congestion/delay increasing as counter-density increases) that respect relevant physical constraints (mass conservation, densities between zero and jam density).

The primary simplification of the model when compared to the physical reality of pedestrian movement is its exclusively longitudinal representation of pedestrian flow. Even though it is possible to combine channels of possibly different width into entire networks, flow and congestion propagation are only one-dimensionally described along the linear channels. A

truly two-dimensional extension is not attempted in the present article, even though it clearly would widen the model's applicability to, e.g., stations or stadiums.

The model's lack of two-dimensional dynamics carries over to its representation of intersections, which are treated as points without spatial extent and without internal dynamics or geometry-dependent effects. For instance, a North→South flow will interact differently with an East→West flow (they need to move through each other) than a North→East flow with a South→West flow (which may move side-by-side through the node). Also, there may be an effect of the angle at which pedestrian streams cross. The model in its current form does not capture such effects; it may be possible to adopt existing extensions from point-like unidirectional vehicular flow models (Corthout et al., 2012; Flötteröd and Rohde, 2011).

CRedit authorship contribution statement

Elhabib Moustaid: Conceptualization, Methodology, Software, Writing - original draft. **Gunnar Flötteröd:** Conceptualization, Methodology, Software, Supervision, Writing - review & editing.

Acknowledgements

This work was partially supported by the PETRA project, funded by the European Commission 7th Framework Programme (FP7-SMARTCITIES-2013) under project number 609042. The anonymous reviewers provided very helpful comments on an earlier version of this document.

Appendix A. Monotonicity of the bidirectional FD

The linear form of the FD over the SR and RS regions renders a more detailed analysis of these regimes unnecessary. Over the SS region, one obtains

$$\frac{d\text{FD}(\varrho \mid \varrho')}{d\varrho} = C \cdot \left((1 + D\hat{v}\varrho)^2 + 2D^2\hat{v}^2\varrho\varrho' - D^2\hat{v}^2(\varrho')^2 \right) \quad (\text{A.1})$$

with $C = \hat{v}/(1 + D\hat{v}(\varrho + \varrho'))^2 > 0$. The SS region is delineated by $\varrho' \leq \varrho^*(\varrho)$. Inserting (2a) and re-arranging yields

$$\frac{d\text{FD}(\varrho \mid \varrho')}{d\varrho} \geq (1 + D\hat{v}\varrho)^2 \cdot \left(1 - \left(\frac{D\hat{v}\hat{\varrho}}{2 + D\hat{v}\hat{\varrho}} \right)^2 \right) + 2D^2\hat{v}^2\varrho\varrho' \quad (\text{A.2})$$

$$> 2D^2\hat{v}^2\varrho\varrho' \geq 0, \quad (\text{A.3})$$

meaning that the FD is strictly monotonously increasing with ϱ over the SS region. From

$$\frac{d\text{FD}(\varrho \mid \varrho')}{d\varrho'} = -2D\hat{v}^2 \cdot \frac{(1 + D\hat{v}\varrho)\varrho}{(1 + D\hat{v}(\varrho + \varrho'))^2} < 0, \quad (\text{A.4})$$

it follows that FD is strictly monotonously decreasing with ϱ' over the SS region.

Appendix B. Proof of Proposition 1

The following two implications of (1), (2a) are needed; see Fig. 1 for geometrical intuition:

$$\varrho \leq \varrho^*(\varrho') \Rightarrow \varrho \leq \hat{\varrho}/2 \quad (\text{B.1})$$

$$\varrho \geq \varrho^*(\varrho') \Rightarrow \varrho' \leq \varrho^*(\varrho). \quad (\text{B.2})$$

The following property of the critical flow as defined in (7a), (7b) is also needed: For all feasible counter-densities ϱ' , one has

$$q^*(\varrho') \geq w\hat{\varrho}/2. \quad (\text{B.3})$$

Let $q_i = \min\{S_{i,l}, R_{i,r}\}$ resp. $q_j = \min\{S_{j,r}, R_{j,l}\}$ be the flow towards the right resp. left in Fig. 4.

Two cases for the link left of the interface are considered.

1. For $\varrho_{j,l} \leq \varrho^*(\varrho_{i,l})$, one has $R_{j,l} \geq w\hat{\varrho}/2$ from (B.3), (10a).
2. For $\varrho_{j,l} \geq \varrho^*(\varrho_{i,l})$, one has $S_{i,l} = w\varrho_{i,l}$ from (B.2), (9b) and $R_{j,l} = w(\hat{\varrho} - \varrho_{j,l})$ from (11c). In combination with (1), this leads to $R_{j,l} \geq S_{i,l}$. Since $q_i \leq S_{i,l}$, one obtains $R_{j,l} \geq q_i$.

Combining these cases leads to

$$R_{j,l} \geq \min\{q_i, w\hat{\varrho}/2\}. \quad (\text{B.4})$$

Three cases for the link right of the interface are considered.

1. For $q_{i,r} \geq \varrho^*(q_{j,r})$, one obtains $R_{i,r} = w(\hat{q} - q_{i,r})$ from (11c) and $S_{j,r} = wq_{j,r}$ from (B.2), (9b). Combined, this leads to $S_{j,r} = R_{i,r} - w(\hat{q} - q_{i,r} - q_{j,r})$.
2. For $q_{i,r} \leq \varrho^*(q_{j,r})$ and $q_{j,r} \leq \varrho^*(q_{i,r})$, one has $R_{i,r} = w(\hat{q} - \varrho^*(q_{j,r}))$ from (B.1), (11a). By under-criticality of $q_{i,r}$, this implies $R_{i,r} \leq w(\hat{q} - q_{i,r})$. Further, the sending flow $S_{j,r}$ is given by (9a). For a given $q_{j,r}$, its minimum value of $wq_{j,r}$ is attained at $q_{i,r} = \varrho^*(q_{j,r})$ due to monotonicity of the sending function. Combining these results leads to $S_{j,r} \geq R_{i,r} - w(\hat{q} - q_{i,r} - q_{j,r})$.
3. For $q_{j,r} \geq \varrho^*(q_{i,r})$, one has $S_{j,r} \geq w\hat{q}/2$ from (B.3), (8b) and $R_{i,r} = w\hat{q}/2$ from (11b). In combination with (1), this leads to $S_{j,r} \geq R_{i,r} \geq R_{i,r} - w(\hat{q} - q_{i,r} - q_{j,r})$.

Given that $q_i \leq R_{i,r}$, all three cases imply

$$S_{j,r} \geq q_i - w(\hat{q} - q_{i,r} - q_{j,r}). \quad (\text{B.5})$$

Combining (B.4) and (B.5) with $q_j = \min\{S_{j,r}, R_{j,l}\}$ leads to

$$q_j \geq \min\{q_i - w(\hat{q} - q_{i,r} - q_{j,r}), w\hat{q}/2\}. \quad (\text{B.6})$$

This expression is further analyzed in two cases.

1. $q_{j,r} \geq \hat{q}/2$. In this case, $R_{i,r} = w\hat{q}/2$ from (11b), which in combination with $q_i \leq R_{i,r}$ implies $q_i - w(\hat{q} - q_{i,r} - q_{j,r}) \leq w\hat{q}/2$. The second argument of the min function in (B.6) hence has no effect.
2. $q_{j,r} \leq \hat{q}/2$. This implies $q_i - w(\hat{q} - q_{i,r} - q_{j,r}) \leq q_i - w(\hat{q} - q_{i,r}) + w\hat{q}/2$. One further obtains $R_{i,r} \leq w(\hat{q} - q_{i,r})$ from (11a) and (11c), which with $q_i \leq R_{i,r}$ again implies that the second argument of the min function in (B.6) has no effect.

Overall, one hence obtains

$$q_i - q_j \leq w(\hat{q} - q_{i,r} - q_{j,r}). \quad (\text{B.7})$$

Noting from (3) that $w \leq \hat{v} \leq \Delta x / \Delta t$, this implies

$$(q_i - q_j) \Delta t \leq (\hat{q} - q_{i,r} - q_{j,r}) \Delta x. \quad (\text{B.8})$$

The l.h.s. of this expression is the amount by which the total occupancy (in pedestrian units) of the right cell is increased. It is not larger than the total available space, which is represented by the r.h.s. The jam density in the right cell can hence not be exceeded. Symmetrical arguments ensure the same for the left cell.

References

- Asano, M., Sumalee, A., Kuwahara, M., Tanaka, S., 2007. Dynamic cell transmission-based pedestrian model with multidirectional flows and strategic route choices. *Transp. Res. Rec. J. Transp. Res. Board* 42–49.
- Blue, V.J., Adler, J.L., 2001. Cellular automata microsimulation for modeling bi-directional pedestrian walkways. *Transp. Res. Part B* 35 (3), 293–312.
- Bode, N.W., Chraïbi, M., Holl, S., 2019. The emergence of macroscopic interactions between intersecting pedestrian streams. *Transp. Res. Part B* 119, 197–210.
- Burstedde, C., Klauck, K., Schadschneider, A., Zittartz, J., 2001. Simulation of pedestrian dynamics using a two-dimensional cellular automaton. *Physica A* 295 (3), 507–525.
- Chen, X., Treiber, M., Kanagaraj, V., Li, H., 2018. Social force models for pedestrian traffic - state of the art. *Transp. Rev.* 38 (5), 625–653. doi:10.1080/01441647.2017.1396265.
- Chraïbi, M., Seyfried, A., Schadschneider, A., 2010. Generalized centrifugal-force model for pedestrian dynamics. *Phys. Rev. E* 82 (4), 046111. doi:10.1103/PhysRevE.82.046111.
- Corthout, R., Flötteröd, G., Viti, F., Tampere, C., 2012. Non-unique flows in macroscopic first-order intersection models. *Transp. Res. Part B* 46 (3), 343–359.
- Daganzo, C.F., 1994. The cell transmission model: a dynamic representation of highway traffic consistent with the hydrodynamic theory. *Transp. Res. Part B* 28 (4), 269–287. doi:10.1016/0191-2615(94)90002-7.
- Dias, C., Lovreglio, R., 2018. Calibrating cellular automaton models for pedestrians walking through corners. *Phys. Lett. A* 382 (19), 1255–1261. doi:10.1016/j.physleta.2018.03.022.
- Feliciani, C., Nishinari, K., 2016. Empirical analysis of the lane formation process in bidirectional pedestrian flow. *Phys. Rev. E* 94 (3), 032304. doi:10.1103/PhysRevE.94.032304.
- Flötteröd, G., Lämmel, G., 2015. Bidirectional pedestrian fundamental diagram. *Transp. Res. Part B* 71, 194–212. doi:10.1016/j.trb.2014.11.001.
- Flötteröd, G., Rohde, J., 2011. Operational macroscopic modeling of complex urban road intersections. *Transp. Res. Part B* 45 (6), 903–922. doi:10.1016/j.trb.2011.04.001.
- Fruin, J., of Urban Designers, M.A., Planners, E., 1971. *Pedestrian Planning and Design*. Metropolitan Association of Urban Designers and Environmental Planners.
- Fu, Z., Yang, L., Rao, P., Zhang, T., 2013. Interactions of pedestrians interlaced in T-shaped structure using a modified multi-field cellular automaton. *Int. J. Mod. Phys. C* 24 (04), 1350024.
- Guo, R.-Y., Huang, H.-J., Wong, S., 2011. Collection, spillback, and dissipation in pedestrian evacuation: a network-based method. *Transp. Res. Part B* 45 (3), 490–506.
- Gupta, A., Pundir, N., 2015. Pedestrian flow characteristics studies: a review. *Transp. Rev.* 35 (4), 445–465. doi:10.1080/01441647.2015.1017866.
- Gärder, P., 1989. Pedestrian safety at traffic signals: a study carried out with the help of a traffic conflicts technique. *Accid. Anal. Prev.* 21 (5), 435–444. doi:10.1016/0001-4575(89)90004-3.
- Helbing, D., Molnar, P., Farkas, I.J., Bolay, K., 2001. Self-organizing pedestrian movement. *Environ. Plann. B* 28 (3), 361–383.
- Helbing, D., Molnár, P., 1995. Social force model for pedestrian dynamics. *Phys. Rev. E* 51 (5), 4282–4286. doi:10.1103/PhysRevE.51.4282.
- Holl, S., 2016. *Methoden für die Bemessung der Leistungsfähigkeit multidirektional genutzter Fußverkehrsanlagen* Doctoral dissertation. Universität Wuppertal, Fakultät für Architektur und Bauingenieurwesen.
- Hussein, M., Sayed, T., 2017. A bi-directional agent-based pedestrian microscopic model. *Transp. A* 13 (4), 326–355. doi:10.1080/23249935.2016.1266531.
- Isobe, M., Adachi, T., Nagatani, T., 2004. Experiment and simulation of pedestrian counter flow. *Physica A* 336 (3), 638–650.
- Lebacque, J., 1996. The Godunov scheme and what it means for first order traffic flow models. In: Lesort, J.-B. (Ed.), *Proceedings of the 13th International Symposium on Transportation and Traffic Theory*. Pergamon, Lyon, France, pp. 647–677.

- Lee, C., Abdel-Aty, M., 2005. Comprehensive analysis of vehicle-pedestrian crashes at intersections in Florida. *Accid. Anal. Prev.* 37 (4), 775–786. doi:10.1016/j.aap.2005.03.019.
- Løvås, G.G., 1994. Modeling and simulation of pedestrian traffic flow. *Transp. Res. Part B* 28 (6), 429–443. doi:10.1016/0191-2615(94)90013-2.
- Peng, Y.-C., Chou, C.-I., 2011. Simulation of pedestrian flow through a "T" intersection: a multi-floor field cellular automata approach. *Comput Phys Commun* 182 (1), 205–208.
- Schadschneider, A., Chraïbi, M., Seyfried, A., Tordeux, A., Zhang, J., 2018. Pedestrian dynamics: from empirical results to modeling. In: Gibelli, L., Bellomo, M. (Eds.), *Crowd Dynamics, Volume 1: Theory, Models, and Safety Problems*. In: *Modeling and Simulation in Science, Engineering and Technology*. Springer International Publishing, Cham, pp. 63–102. doi:10.1007/978-3-030-05129-7_4.
- Schelhorn, T., O'Sullivan, D., Haklay, M., Thurstain-Goodwin, M., 1999. *STREETS: An Agent-Based Pedestrian Model*. Technical Report. Centre for Advanced Spatial Analysis, University College London, England.
- Shukla, P.K., 2010. On modeling and evolutionary optimization of nonlinearly coupled pedestrian interactions. In: Chio, C.D., Cagnoni, S., Cotta, C., Ebner, M., Ekárt, A., Esparcia-Alcazar, A.I., Goh, C.-K., Merelo, J.J., Neri, F., Preuß, M., Togelius, J., Yannakakis, G.N. (Eds.), *Applications of Evolutionary Computation 6024*. In: *Lecture Notes in Computer Science*. Springer Berlin Heidelberg, pp. 21–30.
- Smits, E.-S., Bliemer, M.C.J., Pel, A.J., van Arem, B., 2015. A family of macroscopic node models. *Transp. Res. Part B* 74, 20–39. doi:10.1016/j.trb.2015.01.002.
- Tajima, Y., Nagatani, T., 2002. Clogging transition of pedestrian flow in T-shaped channel. *Physica A* 303 (1), 239–250.
- Tajima, Y., Takimoto, K., Nagatani, T., 2002. Pattern formation and jamming transition in pedestrian counter flow. *Physica A* 313 (3), 709–723.
- Takimoto, K., Tajima, Y., Nagatani, T., 2002. Effect of partition line on jamming transition in pedestrian counter flow. *Physica A* 308 (1), 460–470.
- Thompson, P.A., Marchant, E.W., 1995. A computer model for the evacuation of large building populations. *Fire Saf J* 24 (2), 131–148. doi:10.1016/0379-7112(95)00019-P.
- Turner, A., Penn, A., 2002. Encoding natural movement as an agent-based system: an investigation into human pedestrian behaviour in the built environment. *Environ. Plann. B* 29 (4), 473–490.
- Wang, T., Chen, J., 2009. An improved cellular automaton model for urban walkway bi-directional pedestrian flow. In: *2009 International Conference on Measuring Technology and Mechatronics Automation*, vol. 3, pp. 458–461. doi:10.1109/ICMTMA.2009.252.
- Xie, S., Wong, S., 2015. A Bayesian inference approach to the development of a multidirectional pedestrian stream model. *Transp. A* 11 (1), 61–73.
- Zanlungo, F., Ikeda, T., Kanda, T., 2011. Social force model with explicit collision prediction. *EPL* 93 (6), 68005. doi:10.1209/0295-5075/93/68005.
- Zhang, J., 2012. *Pedestrian fundamental diagrams: Comparative analysis of experiments in different geometries*. Forschungszentrum Jülich Phd dissertation.
- Zhang, J., Klingsch, W., Rupperecht, T., Schadschneider, A., Seyfried, A., 2011a. Empirical study of turning and merging of pedestrian streams in T-junction. arXiv preprint arXiv:1112.5299.
- Zhang, J., Klingsch, W., Schadschneider, A., Seyfried, A., 2011. Transitions in pedestrian fundamental diagrams of straight corridors and T-junctions. *J. Stat. Mech* 2011 (06), P06004.
- Zhang, J., Klingsch, W., Schadschneider, A., Seyfried, A., 2013. Experimental study of pedestrian flow through a T-junction. *Traffic Granular Flow'11* 241–249.
- Zhang, J., Seyfried, A., 2014. Comparison of intersecting pedestrian flows based on experiments. *Physica A* 405, 316–325.
- Zheng, X., Zhong, T., Liu, M., 2009. Modeling crowd evacuation of a building based on seven methodological approaches. *Build Environ* 44 (3), 437–445. doi:10.1016/j.buildenv.2008.04.002.